OCEANOGRAPHY

Southern Ocean anthropogenic carbon sink constrained by sea surface salinity

Jens Terhaar[1,2]*, Thomas L. Frölicher[1,2], Fortunat Joos[1,2]

The ocean attenuates global warming by taking up about one quarter of global anthropogenic carbon emissions. Around 40% of this carbon sink is located in the Southern Ocean. However, Earth system models struggle to reproduce the Southern Ocean circulation and carbon fluxes. We identify a tight relationship across two multimodel ensembles between present-day sea surface salinity in the subtropical-polar frontal zone and the anthropogenic carbon sink in the Southern Ocean. Observations and model results constrain the cumulative Southern Ocean sink over 1850-2100 to 158 ± 6 petagrams of carbon under the low-emissions scenario Shared Socioeconomic Pathway 1-2.6 (SSP1-2.6) and to 279 ± 14 petagrams of carbon under the high-emissions scenario SSP5-8.5. The constrained anthropogenic carbon sink is 14 to 18% larger and 46 to 54% less uncertain than estimated by the unconstrained estimates. The identified constraint demonstrates the importance of the freshwater cycle for the Southern Ocean circulation and carbon cycle.

INTRODUCTION

Anthropogenic carbon (C_{ant}) uptake by the ocean is playing a crucial role in slowing global warming. Since 1850, the global ocean has taken up between 20 and 30% (160 ± 20 Pg of C) of C_{ant} emissions from fossil fuel combustion, cement production, and land-use change (*1, 2*). Around 40% of this global ocean C_{ant} uptake has taken place in the Southern Ocean south of 30°S (*3–9*), making this particular region the largest oceanic sink of C_{ant}.

Observation-based (*5–8*) and model (*9–13*) estimates of the Southern Ocean C_{ant} uptake come with large uncertainties (Fig. 1). The uncertainty in observation-based estimates is mainly caused by data scarcity, especially during wintertime (*14–16*). The uncertainty among models can be attributed to shortcomings in simulating the complex circulation of the Southern Ocean (*11, 17–19*). Observation-based cumulative Southern Ocean C_{ant} fluxes scaled to the period from 1850 to 2005 (see Materials and Methods) range from 40 to 71 Pg of C (*5, 7, 8*), while simulated C_{ant} uptake over the same period ranges from 44 to 63 Pg of C (intermodel range) when using the Earth system models (ESMs) from phase 5 of the Coupled Model Intercomparison Project (CMIP5; fig. S1A) (*9*) and from 43 to 62 Pg of C when using the new CMIP6 model generation (Fig. 1A and Table 1). By 2100, the projected range grows to 194 to 279 Pg of C under the high emissions scenario for CMIP5 [Representative Concentration Pathway 8.5 (RCP8.5) (*20*)] and to 204 to 309 Pg of C under the high emissions scenario for CMIP6 [Shared Socioeconomic Pathway 5-8.5 (SSP5-8.5) (*21*)]. Thus, the new generation of CMIP6 ESMs has, despite further model development and overall increased horizontal and vertical ocean model resolution (*22*), not reduced the uncertainties in Southern Ocean C_{ant} uptake.

In cases of large projection uncertainties, such as for Southern Ocean C_{ant} uptake, the use of emergent constraints offers an opportunity to reduce these uncertainties (*23–25*). Emergent constraints first relate model projections of a particular variable to observable historical trends, sensitivities, or base states of the same or different

variable across an ESM ensemble and then exploit this relationship with observations of the historical trend, sensitivity, or base state. The fidelity of an emergent constraint, thus, depends on the correlation of the relationship and the uncertainty of the observations. Emergent constraints have been applied to constrain many climate-related variables, such as transient (*26, 27*) and equilibrium climate sensitivity (*28, 29*), Arctic snow albedo feedback (*24*), carbon cycle feedbacks (*30, 31*), marine primary production (*32*), and Arctic Ocean acidification (*33*). However, as emergent constraints may conflict with one another (*28, 34*) and can even be derived from data-mined pseudo-correlations (*35*), it is essential to understand and demonstrate the mechanisms that underpin them and to test the identified emergent constraint in an independent model ensemble (*25, 36*).

In this study, we develop and apply an emergent constraint to reduce uncertainties in the Southern Ocean sink of C_{ant}. The constraint relies on observed sea surface salinity. The constraint is supported by physical and biogeochemical process understanding, presented for the CMIP6 ensemble, and confirmed using the CMIP5 ensemble.

Southern Ocean circulation and C_{ant} sink

The important role of the Southern Ocean in the global C_{ant} uptake is due to its unique circulation (*12, 37*). Westerly winds drive a strongly divergent surface flow that allows old Circumpolar Deep Water carrying little C_{ant} to come back to the surface ocean at the polar front (PF), the southern limit of the Antarctic Circumpolar Current (*12, 37, 38*). Only a small fraction of upwelled and surface waters moves southward and is converted into Antarctic Bottom Water (*12, 38*). The largest fraction flows through Ekman transport northward while taking up large amounts of C_{ant} via air-sea gas exchange. Eventually, these northward flowing water masses are transformed to Antarctic Intermediate Water (AAIW) and Subantarctic Mode Water (SAMW) (*38*) via surface heat uptake and mixing with southward flowing water from the mid-latitudes (*15*). AAIW and SAMW, now enriched in C_{ant}, are then subducted in the vicinity of the subtropical front (STF) below the light subtropical waters into the deeper ocean (*38*). The amount of C_{ant} taken up in the Southern Ocean is, thus, primarily dictated by the rate of SAMW and AAIW

[1]Climate and Environmental Physics, Physics Institute, University of Bern, Bern, Switzerland. [2]Oeschger Centre for Climate Change Research, University of Bern, Bern, Switzerland.
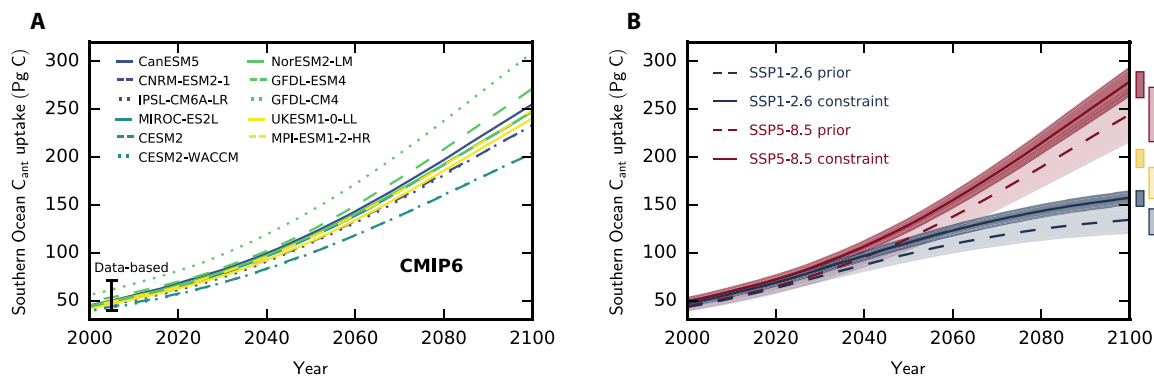*Corresponding author. Email: jens.terhaar@climate.unibe.ch

Fig. 1. Projections of cumulative Southern Ocean C_{ant} uptake in CMIP6. ESM projections of the 21st century Southern Ocean (>30°S) cumulative C_{ant} uptake since 1850 from (**A**) 11 CMIP6 models following the SSP5-8.5 scenario (*21*) with the data-based estimate for cumulative Southern Ocean uptake from 1850 to 2005 (black vertical line) (*5*, *7*, *8*). (**B**) Time series of the multimodel mean C_{ant} uptake under the SSP1-2.6 (blue) and SSP5-8.5 (red) scenarios with ±1 SD for the CMIP6 model ensembles before (transparent) and after the emergent constraint is applied (opaque). The bars indicate the range of ±1 SD of the cumulative C_{ant} uptake in 2100 under SSP1-2.6 (blue), SSP2-4.5 (yellow), and SSP5-8.5 (red) before (transparent) and after (opaque) the constraint is applied.

Table 1. Unconstrained (prior) and constrained (after constraint) cumulative Southern Ocean C_{ant} uptake (petagrams of C) in CMIP5 and CMIP6*.

Simulations	Prior	After constraint
CMIP6		
Historical		
1850–2005	49 ± 5	55 ± 3
1850–2014	58 ± 6	65 ± 4
SSP1–2.6		
1850–2100	134 ± 13	158 ± 6
2015–2100	78 ± 10	96 ± 4
SSP2-4.5		
1850–2100	173 ± 16	200 ± 8
2015–2100	117 ± 12	138 ± 6
SSP5-8.5		
1850–2100	245 ± 28	278 ± 13
2015–2100	187 ± 22	214 ± 11
CMIP5[†]		
Historical		
1850-2005	51 ± 5	53 ± 4
RCP2.6		
1850–2100	138 ± 10	142 ± 6
2006–2100	86 ± 8	88 ± 7
RCP4.5		
1850–2100	174 ± 15	183 ± 7
2006–2100	122 ± 12	129 ± 7
RCP8.5		
1850–2100	241 ± 24	253 ± 9
2006–2100	190 ± 21	200 ± 10

*Not all models were available for all future scenarios so that historical and future estimates do not always add up exactly to the estimates of the full period.   †GFDL-ESM2M and GFDL-ESM2G simulations started in 1861.

formation with other factors, such as the buffer capacity of surface waters and the air-sea equilibration time of CO_2, being less important (*3*, *4*, *9*, *19*, *39*, *40*).

The total subduction rate of SAMW and AAIW depends on the density of the northward flowing surface waters (*41*, *42*) and on the density structure of the upper ocean (*12*, *17*). Heavier surface waters, corresponding to larger outcrop areas of SAMW and AAIW (fig. S1C) (*41*), have the potential to penetrate deeper and to occupy a larger volume below the surface than lighter waters (*12*, *42*). Similarly, surface waters penetrate more easily when density increases weakly with depth than in a strongly stratified ocean. Across the CMIP6 and CMIP5 model ensembles the volume of ocean interior water ventilated by surface waters that lies between the PF and the STF, namely, SAMW and AAIW, increases with increasing sea surface density ($r^2 = 0.74$; figs. S2 to S5). Sea surface density is, thus, a physically supported indicator of the formation rate of SAMW and AAIW (*12*, *41*, *43*, *44*) and, in turn, of C_{ant} uptake by the Southern Ocean (*12*, *41*).

The sea surface density variations in the cold Southern Ocean depends strongly on variations in surface salinity ($r^2 = 0.84$; fig. S2A) (*13*, *42–45*) and less on variations in surface temperature ($r^2 = 0.01$; fig. S2B). The salinity at the surface is influenced by the hydrological balance of evaporation minus precipitation, sea and land ice melt, and net salinity transport into the surface layers via circulation. This balance of complex and intricate processes and, in turn, surface salinity and density is difficult to represent correctly in models (*10*, *17*, *18*, *46*). In CMIP5 models, for example, the Southern Ocean surface waters were found to have on average a fresh bias (fig. S2A) (*10*, *17*, *18*), but the model spread is substantial. A negative salinity bias is possibly caused by too much precipitation (*47*), too little subsurface inflow of Circumpolar Deep Water into the Southern Ocean (*17*), too weak and equatorward displaced winds that therefore do not create enough upwelling (*48*), and a too large decline of the sea ice extent over the past decades (*46*). Nevertheless, the outlined mechanistic explanation supported by the above presented model results suggests that sea surface salinity in the Southern Ocean is a strong and well observable indicator of SAMW and AAIW formation and, hence, C_{ant} uptake.

RESULTS

Emergent relationship between Southern Ocean sea surface salinity and C_{ant} uptake

A tight relationship between Southern Ocean sea surface salinity and C_{ant} uptake is found for the CMIP5 and CMIP6 models. ESMs, such as the Community Earth System Model version 2 (CESM2), that simulate low mean surface salinities (and densities) between the PF and the STF also simulate a small C_{ant} uptake in the Southern Ocean south of 30°S, while ESMs that simulate high salinities, such as the Geophysical Fluid Dynamics Laboratory's CM4.0 physical climate model (GFDL-CM4), also simulate a high C_{ant} uptake (Fig. 2 and figs. S6 and S7). We, therefore, expect and find a strong correlation between the cumulative C_{ant} uptake and the mean of present-day sea surface salinity between the PF and STF averaged over 1986–2005. This correlation holds across the two latest model generations (CMIP6 and CMIP5) and for every year of the 21st century (Fig. 3 and figs. S8 and S9, A and B). This relation yields, when combined with observations of sea surface salinity, a so-called emergent constraint (11, 36) on the cumulative C_{ant} uptake in the Southern Ocean across 11 ESMs from CMIP6 (Fig. 3) and across 13 ESMs from CMIP5 (fig. S8).

Southern Ocean cumulative C_{ant} uptake since 1850 was calculated for each ESM as the difference between the cumulative air-sea CO_2 flux south of 30°S between the historical and future simulation and the corresponding preindustrial control (pi-Control) simulation. This definition of C_{ant} uptake includes the flux driven by increasing atmospheric CO_2 concentrations and the changes in the natural air-sea CO_2 flux due to climate change (e.g., warming and changes in circulation and biology). The PF and STF were identified for each

month and each longitude by the maximum temperature gradients based on the sea surface temperature over 1986–2005 for each model (49–51) (see Materials and Methods and fig. S10) to compute mean surface salinity from monthly data for this frontal region. One ensemble member was used per ESM as internal model variability is small compared to the differences between models (see Materials and Methods). The relationship between the cumulative C_{ant} uptake and the mean surface salinity between the PF and STF was calculated using a linear regression with equal weight for each model. The constrained estimate of the cumulative C_{ant} uptake is then calculated as the normalized product of the conditional probability density functions (PDFs) of the emergent relationship and the observations assuming Gaussian distributions.

With this emergent constraint, the Southern Ocean cumulative C_{ant} uptake from 1850 to 2005 of the CMIP6 model ensemble changes from 49 ± 5 to 55 ± 3 Pg of C (r^2 = 0.74; Table 1 and Fig. 3) (the uncertainty refers to ±1 SD, and r^2 is the coefficient of determination between simulated sea surface salinity and C_{ant} uptake). The unconstrained and constrained mean estimates are significantly different (Student's t test, 5% significance level). The constrained mean estimate is also closer to the central value of the observation-based estimates of 58 ± 13 Pg of C (5, 7) and 54 ± 14 Pg of C (8) over the same period.

Constrained cumulative C_{ant} uptake from 1850 to 2100 in CMIP6

After applying the emergent constraint to the cumulative Southern Ocean C_{ant} uptake from 1850 to 2100, the uptake changes from
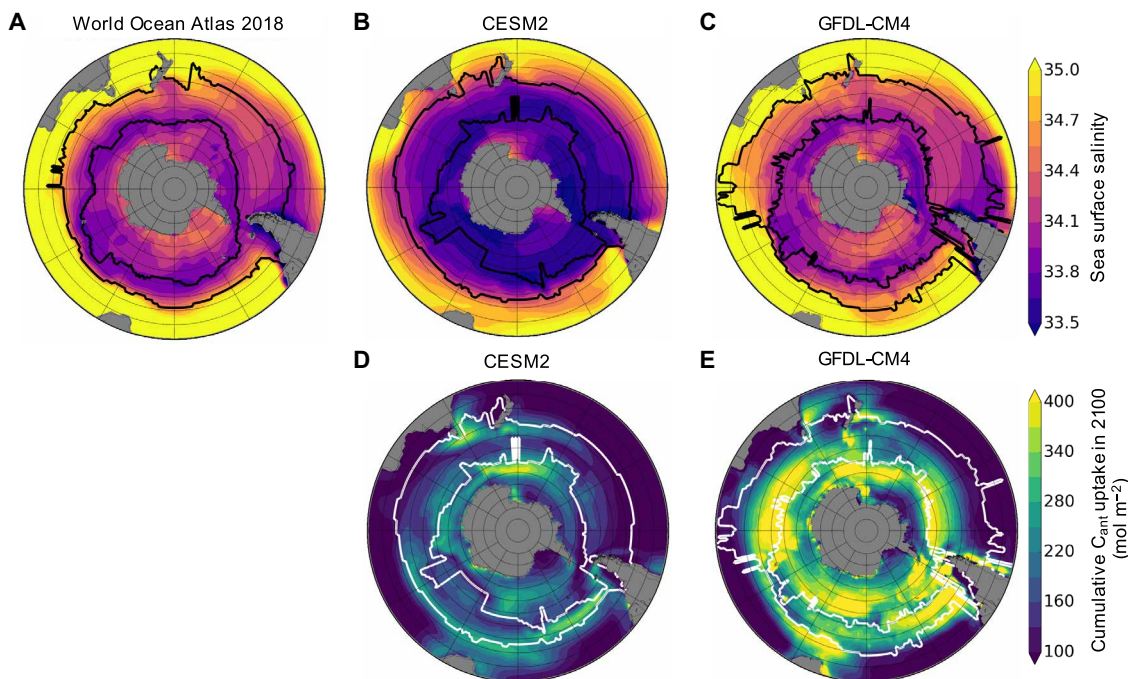
Fig. 2. Sea surface salinity and cumulative C_{ant} uptake in the Southern Ocean. (**A**) Present-day sea surface salinity in August from World Ocean Atlas 2018 (80) and the sea surface salinity in August averaged over 1986–2005 simulated by the (**B**) CESM2 and (**C**) GFDL-CM4 models. Both models are part of CMIP6. Black and white contour lines delineate the PF and the STF in August. Simulated cumulative Southern Ocean (>30°S) C_{ant} uptake over 1850–2100 for the (**D**) CESM2 and (**E**) GFDL-CM4 models. CESM2 is the minimum of the CMIP6 ensemble for both present-day (1986–2005) mean sea surface salinity between the PF and STF (33.67) and projected cumulative C_{ant} uptake in 2100 (204 Pg of C), while GFDL-CM4 is the ensemble maximum (34.16 and 309 Pg of C). The observation-based mean sea surface salinity between the PF and STF is 34.07 [World Ocean Atlas 2018 (80)].
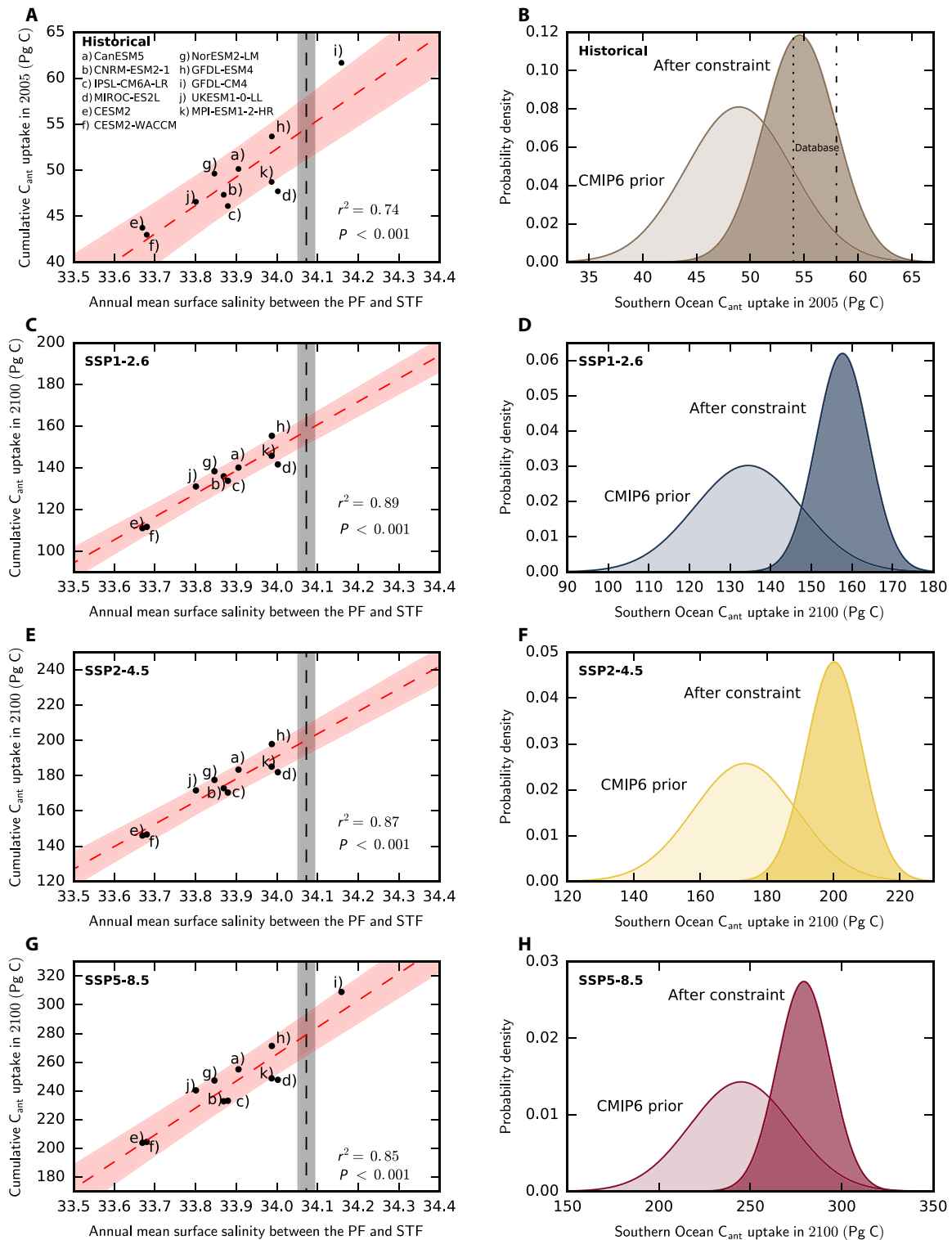
Fig. 3. Emergent constraints on the cumulative Southern Ocean C_ant uptake in CMIP6. The projected cumulative C_ant uptake in the Southern Ocean south of 30°S across the CMIP6 model ensemble for (**A**) the historical period from 1850 to 2005, and the historical and future period from 1850 to 2100 under (**C**) SSP1-2.6, (**E**) SSP2-4.5, and (**G**) SSP5-8.5 against the present-day (1986–2005) mean sea surface salinity between the PF and STF. Linear regression fits (red dashed lines) and the associated 68% prediction intervals are shown in (A), (C), (E), and (G), as are observation-based estimates of present-day annual sea surface density between the PF and STF (black dashed lines) with the associated uncertainty (black shaded area). Probability density functions for the cumulative Southern Ocean C_ant uptake from (**B**) 1850 to 2005 and from 1850 to 2100 under (**D**) SSP1-2.6, (**F**) SSP2-4.5, and (**H**) SSP5-8.5, before ("CMIP6 prior," transparent) and after ("after constraint," opaque) the emergent constraint is applied. Data-based estimates are shown in (B) as dash-dotted (*5*, *7*) and dotted (*8*) lines and are scaled to the same definition of C_ant as the models (see Materials and Methods).

134 ± 13 to 158 ± 6 Pg of C ($r^2 = 0.89$; Table 1 and Fig. 3) under the low emissions SSP1-2.6 scenario. For the SSP2-4.5 scenario with moderate CO_2 emissions, which peak in the middle of the 21st century and decrease afterward, the Southern Ocean cumulative C_{ant} uptake changes from 173 ± 16 to 200 ± 8 Pg of C ($r^2 = 0.87$). Under the high emissions scenario SSP5-8.5, the Southern Ocean cumulative C_{ant} uptake changes from 244 ± 28 to 278 ± 13 Pg of C ($r^2 = 0.85$). Thus, the uncertainty of the estimated cumulative C_{ant} uptake in 2100 is reduced by 46 to 54% across these three CMIP6 scenarios, while the estimated uptake itself is increased by 14 to 18%. Across the CMIP6 ensemble, 10 of 11 ESMs underestimate the annual sea surface salinity between the PF and STF and, therefore, also the uptake of C_{ant}. By correcting for this systematic sea surface salinity bias, the constrained Southern Ocean cumulative C_{ant} uptake in 2100 is significantly (Student's t test, 5% significance level) larger than the unconstrained uptake in each scenario.

Comparison to CMIP5

To test the robustness of the emergent constraint, we further applied the constraint to the CMIP5 model ensemble. In this ensemble, the cumulative Southern Ocean C_{ant} uptake from 1850 to 2100 changes from 138 ± 10 to 142 ± 6 Pg of C under the low emissions RCP2.6 scenario ($r^2 = 0.77$), from 173 ± 16 to 183 ± 8 Pg of C under the moderate emissions RCP4.5 scenario ($r^2 = 0.88$), and from 241 ± 24 to 253 ± 9 Pg of C under the high emissions RCP8.5 scenario ($r^2 = 0.90$) (fig. S8).

As for the CMIP6 model ensemble, the uncertainty of the constrained estimates is approximately half (40 to 63%) of the uncertainty of the unconstrained estimate. The increase in the best estimate in the constrained results of the CMIP5 ensemble, however, is with 3 to 6% not significant (Student's t test, 5% significance level) and smaller than the relative increase in the CMIP6 model ensemble (14 to 18%). This smaller change in the best estimate is due to a smaller model-averaged mean salinity bias in CMIP5 (0.11) than in CMIP6 (0.18).

The Southern Ocean C_{ant} uptake is generally smaller for RCPs than for their SSP counterparts. This difference is to a large extent caused by higher prescribed atmospheric CO_2 trajectories over the 21st century in the SSP than in the RCP scenarios, due to different energy and land use assumptions (20, 21). In the high emissions scenarios, for example, prescribed anthropogenic CO_2 in the atmosphere is, on average over the 21st century, around 15% larger in SSP5-8.5 than in RCP8.5 (52, 53). This explains to a large extent why the constrained cumulative Southern Ocean C_{ant} uptake from 2005 to 2100 is 12% larger for SSP5-8.5 than for RCP8.5 (Table 1).

Extending the constraint to Southern Ocean acidification?

Our emergent constraint suggests that the Southern Ocean may take up more C_{ant} than estimated by the CMIP6 model mean. However, enhanced C_{ant} uptake may also cause stronger ocean acidification (54), i.e., a decrease in pH and in the saturation state of seawater relative to the calcium carbonate mineral aragonite (Ω_{arag}) and calcite (Ω_{calc}). These changes in seawater chemistry have been shown to negatively affect keystone aragonite and calcite shell-forming species and other marine organisms (55–57).

By extending the emergent constraint approach from C_{ant} uptake to ocean acidification at different depth levels (33) in the Southern Ocean, we project slightly greater ocean acidification across the CMIP6 model ensemble north of the STF between 30°S and 40°S, where most of the subducted AAIW and SAMW are located (fig. S11). In

waters between 300 and 1500 m, end-of-century Ω_{arag} under SSP5-8.5 projected by the CMIP6 model ensemble is reduced by the constraint from 0.78 ± 0.06 to 0.74 ± 0.06, and Ω_{calc} is reduced by the constraint from 1.22 ± 0.09 to 1.16 ± 0.10. Constrained end-of-century Ω_{arag} and Ω_{calc} projections are only significantly different (Student's t test, 5%) from the unconstrained projections between 300 and 600 m. Below 1500 m where SAMW and AAIW do not occur (17), there is no relationship between sea surface salinity between the PF and STF and end-of-century Ω_{arag} and Ω_{calc}.

Compared to the emergent constraint on cumulative Southern Ocean C_{ant}, constraining Ω_{arag} and Ω_{calc} with sea surface salinity does not reduce the uncertainties in Ω_{arag} and Ω_{calc} and only very slightly adjusts the best estimate. While sea surface salinity was shown to constrain the C_{ant} uptake from the atmosphere, it does not constrain other processes that influence Ω_{arag} and Ω_{calc}, such as the interior ocean C_{ant} transport from the Southern Ocean to the subtropics, which varies strongly across models (9), and changes in alkalinity, nutrients, temperature, and salinity.

DISCUSSION

Potential limitations

Use of emergent constraints has limits when important processes for the identified relationship are not included or poorly represented in ESMs (25). In this section, the possible role of mesoscale eddies, freshwater input from Antarctic ice melt, acceleration of the Southern Ocean meridional overturning circulation, and biological processes are discussed.

Mesoscale eddies in the Southern Ocean influence the transport of tracers, such as heat, salinity, carbon, and nutrients (58–61). However, the explicit simulation of these mesoscale eddies requires high horizontal and vertical ocean model resolutions, especially in high latitudes such as the Southern Ocean (62). Most of the CMIP5 and CMIP6 models use ocean models with horizontal resolution of about 1° (22, 63). To date, conducting transient simulations with fully coupled ESMs in higher resolution is computationally too expensive, especially because these simulations also need a sufficiently long spin-up to reach a stable equilibrium (64, 65). Therefore, the effect of eddies on the mean ocean circulation and the transport of ocean tracers, such as salinity and carbon, are parametrized within the CMIP models. While the eddy parametrization has an effect on the simulated sea surface salinity and C_{ant} uptake (58–61), this effect cannot be quantified by the state-of-the art CMIP6 ESMs due to their relatively coarse resolution and merits further investigation when eddy-resolving ocean models incorporated in global coupled ESMs will become more widely available.

Furthermore, changes in freshwater input from Antarctic ice melt are not included in any of these models. This freshwater input has the potential to further reduce sea surface salinity and, thus, the uptake of C_{ant} in the Southern Ocean. Although the effect of land ice melt on the sea surface salinity between the PF and STF in recent decades (estimated to be <0.05 over 1995–2015) (66) is small compared to the present day (1986–2005) intermodel variability (0.8; Fig. 3 and fig. S2A), more research is needed to quantify the effect of land ice melt over the 21st century.

Another observed process that is not well represented by the models is the acceleration of the upper cell of the Southern Ocean meridional overturning circulation in the past decades (67). This acceleration and potential further acceleration in the future might

reduce the residence time of waters at the surface below the around 10 months that are necessary for surface ocean partial pressure of CO_2 to equilibrate with the atmosphere and, thus, potentially reduce the uptake of C_{ant} from the atmosphere (15).

In addition, our emergent constraint is purely physical and does not account for the representation of biological processes and their potential changes over the 21st century, which varies largely among these models (68, 69). However, recent studies (70, 71) have suggested that biological processes, in comparison to ocean physics, currently play a minor role for the oceanic C_{ant} uptake despite their importance for natural CO_2 air-sea fluxes (72).

"Confirmed" emergent constraint

The development and increasing use of emergent constraints in recent years not only led to major advances in the understanding of the Earth system but also led to conflicting results, i.e., emergent constraints for the same projected variable, but different observable variables led to different results (28, 34). Moreover, it is shown that in a large dataset such as the CMIP dataset, emergent constraints can be derived even from data-mined pseudo-correlations (35). To avoid spurious constraints, Hall et al. (25) propose three criteria for emergent constraints to be confirmed. These criteria are (i) a plausible mechanism behind the emergent relationship, (ii) verification of the proposed mechanism, (iii) and out-of-sample testing. All three criteria are met in our analysis.

First, we proposed a plausible underlying mechanism, namely, that the Southern Ocean sea surface salinity determines the amount of SAMW and AAIW that is subducted below the surface ocean and thereby the transport of C_{ant} from the surface to the subsurface ocean. The more C_{ant} is removed from the surface ocean, the more C_{ant} can be taken up from the atmosphere via air-sea CO_2 flux. Second, we verified this mechanism by demonstrating that the salinity in the frontal region is related to the outcrop area of SAMW and AAIW and to the volume of ventilated waters in the subsurface Southern Ocean and to C_{ant} uptake (figs. S2 to S5). Third, we applied out of sampling testing across a different ESM ensemble (CMIP5). Although models in new CMIP generations are not strictly independent from their predecessors from which they were developed, this out-of-sample testing in a previous model generation is regarded as useful evidence of an underlying emergent constraint (25).

While the relationship between the volume of subducted SAMW and AAIW and the Southern Ocean C_{ant} uptake might be more direct, we chose the sea surface salinity as the observable quantity because its observations are less uncertain. Sea surface salinity provides the best compromise between a good linear correlation and low observational uncertainties.

Our results do not directly constrain the C_{ant} uptake of the global ocean. The Southern Ocean C_{ant} uptake over 1850–2100 south of 30°S is not correlated to the ocean C_{ant} sink north of 30°S ($r^2 = 0.07$), i.e., a weak or strong Southern Ocean C_{ant} sink is not systematically compensated by a strong or weak C_{ant} sink north of 30°S. Thus, intermodel differences in the C_{ant} uptake north of 30°S remain unchanged.

The importance of the Southern Ocean freshwater cycle

Our results suggest that the simulation of sea surface salinity and of the cumulative Southern Ocean C_{ant} uptake are in better agreement with observations in the CMIP5 model ensemble than in the new CMIP6 model ensemble. This is unexpected as the ocean's vertical and horizontal resolution is increased from CMIP5 to CMIP6 in almost all ESMs (22) and the representation of the wind forcing and sea surface temperature in the Southern Ocean is improved (73). However, large biases with respect to the freshwater cycle and the sea surface salinity remain or even increased from CMIP5 to CMIP6. We show that it is indeed sea surface salinity and the freshwater cycle in the Southern Ocean that is crucial for simulating the Southern Ocean circulation (74, 75) and the associated ocean C_{ant} uptake (45, 76). An improved ability to properly simulate the Southern Ocean freshwater cycle is urgently needed to pin down one of the largest uncertainties in projections of the fate of C_{ant} and the climate.

MATERIALS AND METHODS
Earth system models
We used 24 ESMs in this study, 11 from the CMIP6 (table S1), and 13 from the CMIP5. All models include coupled ocean biogeochemistry schemes and have been applied within the context of both climate and ocean biogeochemical projections (68, 69). A single ensemble member of the concentration-driven simulations was used for each ESM (ensemble member 1 was used when available, otherwise ensemble member 2 was used). All model simulations cover the period 1850 to 2100 (1861–2100 for the GFDL-ESM2G and GFDL-ESM2M, respectively) following historical greenhouse gas and aerosol and natural forcing changes over the period 1850–2005 (CMIP5) or 1850–2014 (CMIP6). For CMIP5 models, the simulations follow RCP2.6, RCP4.5, and RCP8.5 over 2006–2100, and for CMIP6, they follow SSP1-2.6, SSP2-4.5, and SSP5-8.5 over 2015–2100. GFDL-CM4 output was only available for SSP5-8.5, Centro Euro-Mediterraneo sui Cambiamenti Climatici - Community Earth System Model (CMCC-CESM) output only for RCP8.5, and Hadley Centre Global Environment Model version 2 - Carbon Cycle (HadGEM2-CC) and Community Earth System Model version 1–Biogeochemistry (CESM1-BGC) output only for RCP4.5 and RCP8.5.

Simulated annual air-sea CO_2 flux and monthly temperature and salinity output fields south of 30°S were used. All these output fields were analyzed on the native model grid. The anthropogenic air-sea CO_2 flux was calculated as the difference between the air-sea CO_2 flux in historical simulations merged with the future simulations and the concurrent pi-Control simulations. Hence, any model drift was directly accounted for. Note that this definition of the anthropogenic air-sea CO_2 flux includes both the flux driven by increasing atmospheric CO_2 concentrations and any flux from changes in the natural air-sea CO_2 flux. Changes in the natural air-sea CO_2 flux may arise from climate change driven by anthropogenic and natural forcing and internal climate variability.

The mean Southern Ocean sea surface salinity between the PF and STF was calculated for each ESM based on a monthly climatology of sea surface temperature and salinity outputs from 1986 to 2005. Throughout the manuscript, salinity is reported on the Practical Salinity Scale. The fronts were identified for each month, longitude, and model by the maximum latitudinal temperature gradients over a temperature range from 1° to 6°C in the case of the PF and a range from 9° to 18°C in the case of the STF across the entire model ensemble (fig. S10) (49–51). The monthly area-averaged salinities between the fronts were then averaged to obtain an annual mean. Our definition of the fronts leads sometimes to large shifts in the latitudinal position (fig. S10). However, our results are insensitive to the definition of the fronts. Even if the fronts are chosen over a wider range of isotherms, the emergent constraint remains robust (table S2).

Ω_{arag} and Ω_{calc} were calculated offline from simulated dissolved inorganic carbon, total alkalinity, temperature, salinity, and, where available, dissolved inorganic phosphorus and silicon using mocsy2.0 (77) and the equilibrium constants recommended for best practices (78). To account for carbonate chemistry biases in the present-day mean state of the ESMs, model anomalies of all input variables relative to 2002 were added to the observation-based Global Ocean Analysis Project version 2 (GLODAPv2) observational product (79), which is normalized to the year 2002. For models without dissolved inorganic phosphorus and silicon output, anomalies were assumed to be zero. Model anomalies were corrected for potential model drift using concurrent pi-Control simulations. All grid cells with GLODAPv2 observational coverage (~96% of Southern Ocean volume) were used. Basin-wide averages between 30°S and 40°S of Ω_{arag} and Ω_{calc} were weighted on the basis of grid cell volumes.

The role of internal model variability
The influence of the model internal variability on the detected emergent constraint was assessed using the first four ensemble members of the Institut Pierre-Simon Laplace - Climate Model 6A - Low Resolution (IPSL-CM6A-LR). The internal variabilities of present-day annual sea surface density between the PF and STF (33.85 to 33.88) and the projected cumulative C_{ant} uptake in the Southern Ocean (233.2 to 234.6 Pg of C) were found to be negligible in comparison with the range across the CMIP5 and CMIP6 model ensembles (33.56 to 34.34; 194 to 309 Pg of C).

Observational constraints
The sea surface salinity between the PF and STF was calculated identically as for the ESM ensemble but using observation-based sea surface salinities and temperatures from the World Ocean Atlas 2018 climatologies (80). The uncertainty associated with the sea surface salinity was estimated using the area-averaged SE of the sea surface salinity of the World Ocean Atlas 2018 in every surface grid cell within the region.

Observation-based C_{ant} fluxes
The observation-based cumulative C_{ant} fluxes from 1850 to 2005 were derived from observation-based C_{ant} fluxes for the year 1995 [1.12 ± 0.26 Pg of C year^{-1} (5, 7) and 1.04 ± 0.27 Pg of C year^{-1} (8)]. Following standard practice (5, 7, 8, 81), the C_{ant} flux for a year t was derived from the observation-based C_{ant} fluxes in 1995 by scaling the flux proportional to the anthropogenic CO_2 concentration in the atmosphere

$$F_{ant}^{1765}(t) = F_{ant}^{1765}(1995)\frac{\Delta CO_2^{1765}(t)}{\Delta CO_2^{1765}(1995)} \qquad (1)$$

with t being the respective year, F_{ant}^{1765} being the C_{ant} flux into the ocean relative to year 1765, and $\Delta CO_2^{1765}(t)$ being the perturbation in the CO_2 mixing ratio in the atmosphere relative to 1765 [e.g., for year 1995, it is 82 parts per million (ppm) = 360 ppm − 278 ppm].

CMIP5 and CMIP6 models start in the year 1850 and therefore define all C_{ant} emitted after 1850 as C_{ant} , while observation-based estimates commonly define C_{ant} as all C_{ant} emitted after 1765. This different definition of C_{ant} leads to an underestimation of C_{ant} by ESMs when compared to observation-based estimates for two reasons: The time during which the ocean takes up C_{ant} is reduced by

85 years, and the difference in the natural background CO_2 concentration is around 7 ppm (82). When combined, this has been found to yield a difference in the global ocean cumulative C_{ant} uptake of 29 Pg of C by 1995 (29%) (82).

To be able to compare model results to observation-based estimates, we scaled the observation-based estimate of the C_{ant} fluxes to the C_{ant} definition that is used in the ESMs using the following equation

$$F_{ant}^{1850}(t) = F_{ant}^{1765}(1995)\frac{\Delta CO_2^{1850}(t)}{\Delta CO_2^{1765}(1995)} \qquad (2)$$

with F_{ant}^{1850} and F_{ant}^{1765} being the C_{ant} flux into the ocean estimated from measurements relative to the reference year 1850 and 1765, respectively, ΔCO_2^{1850} being the perturbation in the CO_2 mixing ratio in the atmosphere relative to 1850 as used by the ESMs, and ΔCO_2^{1765} being the perturbation in the CO_2 mixing ratio in the atmosphere relative to 1765 as used by the observation-based estimates. By doing so, the observation-based estimates of cumulative Southern Ocean C_{ant} uptake from 1765 to 2005 are reduced by 25% for the period 1850 to 2005, e.g., from 77 to 58 Pg of C (5, 7) and from 72 to 54 Pg of C (8).

Emergent constraints
For the emergent constraints, a linear regression was calculated between the projected variable (C_{ant} uptake or Ω_{arag} and Ω_{calc}) and the sea surface salinity between the PF and STF. All models were weighted equally. PDFs of the projected variable were calculated for the unconstrained (prior) ensemble and the emergent constraints. The prior PDF was derived assuming all models were equally likely and sampled from a Gaussian distribution. The constrained PDFs were calculated as the normalized product of the conditional PDF of the emergent relationship and the PDF of the observational constraint following previously established methodologies (26, 27, 29–33).

SUPPLEMENTARY MATERIALS
Supplementary material for this article is available at http://advances.sciencemag.org/cgi/content/full/7/18/eabd5964/DC1

View/request a protocol for this paper from *Bio-protocol*.

REFERENCES AND NOTES
1. P. Friedlingstein, M. W. Jones, M. O'Sullivan, R. M. Andrew, J. Hauck, G. P. Peters, W. Peters, J. Pongratz, S. Sitch, C. Le Quéré, D. C. E. Bakker, J. G. Canadell, P. Ciais, R. B. Jackson, P. Anthoni, L. Barbero, A. Bastos, V. Bastrikov, M. Becker, L. Bopp, E. Buitenhuis, N. Chandra, F. Chevallier, L. P. Chini, K. I. Currie, R. A. Feely, M. Gehlen, D. Gilfillan, T. Gkritzalis, D. S. Goll, N. Gruber, S. Gutekunst, I. Harris, V. Haverd, R. A. Houghton, G. Hurtt, T. Ilyina, A. K. Jain, E. Joetzjer, J. O. Kaplan, E. Kato, K. K. Goldewijk, J. I. Korsbakken, P. Landschützer, S. K. Lauvset, N. Lefèvre, A. Lenton, S. Lienert, D. Lombardozzi, G. Marland, P. C. McGuire, J. R. Melton, N. Metzl, D. R. Munro, J. E. M. S. Nabel, S.-I. Nakaoka, C. Neill, A. M. Omar, T. Ono, A. Peregon, D. Pierrot, B. Poulter, G. Rehder, L. Resplandy, E. Robertson, C. Rödenbeck, R. Séférian, J. Schwinger, N. Smith, P. P. Tans, H. Tian, B. Tilbrook, F. N. Tubiello, G. R. van der Werf, A. J. Wiltshire, S. Zaehle, Global carbon budget 2019. *Earth Syst. Sci. Data* **11**, 1783–1838 (2019).
2. S. Khatiwala, T. Tanhua, S. Mikaloff Fletcher, M. Gerber, S. C. Doney, H. D. Graven, N. Gruber, G. A. McKinley, A. Murata, A. F. Ríos, C. L. Sabine, Global ocean storage of anthropogenic carbon. *Biogeosciences* **10**, 2169–2191 (2013).
3. C. L. Sabine, R. A. Feely, N. Gruber, R. M. Key, K. Lee, J. L. Bullister, R. Wanninkhof, C. S. Wong, D. W. Wallace, B. Tilbrook, F. J. Millero, T. H. Peng, A. Kozyr, T. Ono, A. F. Rios, The oceanic sink for anthropogenic CO_2. *Science* **305**, 367–371 (2004).
4. K. Caldeira, P. B. Duffy, The role of the Southern Ocean in uptake and storage of anthropogenic carbon dioxide. *Science* **287**, 620–622 (2000).
5. S. E. Mikaloff Fletcher, N. Gruber, A. R. Jacobson, S. C. Doney, S. Dutkiewicz, M. Gerber, M. Follows, F. Joos, K. Lindsay, D. Menemenlis, A. Mouchet, S. A. Müller, J. L. Sarmiento, Inverse estimates of anthropogenic CO_2 uptake, transport, and storage by the ocean. *Glob. Biogeochem. Cycles* **20**, GB2002 (2006).

6. T. DeVries, The oceanic anthropogenic CO_2 sink: Storage, air-sea fluxes, and transports over the industrial era. *Glob. Biogeochem. Cycles* **28**, 631–647 (2014).

7. N. Gruber, M. Gloor, S. E. Mikaloff Fletcher, S. C. Doney, S. Dutkiewicz, M. J. Follows, M. Gerber, A. R. Jacobson, F. Joos, K. Lindsay, D. Menemenlis, A. Mouchet, S. A. Müller, J. L. Sarmiento, T. Takahashi, Oceanic sources, sinks, and transport of atmospheric CO_2. *Glob. Biogeochem. Cycles* **23**, GB1005 (2009).

8. M. Gerber, F. Joos, M. Vázquez-Rodríguez, F. Touratier, C. Goyet, Regional air-sea fluxes of anthropogenic carbon inferred with an ensemble Kalman filter. *Glob. Biogeochem. Cycles* **23**, GB1013 (2009).

9. T. L. Frölicher, J. L. Sarmiento, D. J. Paynter, J. P. Dunne, J. P. Krasting, M. Winton, Dominance of the Southern Ocean in anthropogenic carbon and heat uptake in CMIP5 models. *J. Clim.* **28**, 862–886 (2015).

10. A. J. S. Meijers, The Southern Ocean in the Coupled Model Intercomparison Project phase 5. *Phil. Trans. R. Soc. A* **372**, 20130296 (2014).

11. A. Kessler, J. Tjiputra, The Southern Ocean as a constraint to reduce uncertainty in future ocean carbon sinks. *Earth Syst. Dynam.* **7**, 295–312 (2016).

12. B. K. Mignone, A. Gnanadesikan, J. L. Sarmiento, R. D. Slater, Central role of Southern Hemisphere winds and eddies in modulating the anthropogenic carbon. *Geophys. Res. Lett.* **33**, L01604 (2006).

13. T. DeVries, C. Le Quéré, O. Andrews, S. Berthet, J. Hauck, T. Ilyina, P. Landschützer, A. Lenton, I. D. Lima, M. Nowicki, J. Schwinger, R. Séférian, Decadal trends in the ocean carbon sink. *Proc. Natl. Acad. Sci. U.S.A.* **116**, 11646–11651 (2019).

14. J. D. Majkut, B. R. Carter, T. L. Frölicher, C. O. Dufour, K. B. Rodgers, J. L. Sarmiento, An observing system simulation for Southern Ocean carbon dioxide uptake. *Phil. Trans. R. Soc. A* **372**, 20130046 (2014).

15. N. Gruber, P. Landschützer, N. S. Lovenduski, The variable Southern Ocean carbon sink. *Annu. Rev. Mar. Sci.* **11**, 159–186 (2019).

16. S. M. Bushinsky, P. Landschützer, C. Rödenbeck, A. R. Gray, D. Baker, M. R. Mazloff, L. Resplandy, K. S. Johnson, J. L. Sarmiento, Reassessing Southern Ocean air-sea CO_2 flux estimates with the addition of biogeochemical float observations. *Glob. Biogeochem. Cycles* **33**, 1370–1388 (2019).

17. J.-B. Sallée, E. Shuckburgh, N. Bruneau, A. J. S. Meijers, T. J. Bracegirdle, Z. Wang, T. Roy, Assessment of Southern Ocean water mass circulation in CMIP5 models: Historical bias and forcing response. *J. Geophys. Res.* **118**, 1830–1844 (2013).

18. J.-B. Sallée, E. Shuckburgh, N. Bruneau, A. J. S. Meijers, T. J. Bracegirdle, Z. Wang, Assessment of Southern Ocean mixed-layer depths in CMIP5 models: Historical bias and forcing response. *J. Geophys. Res.* **118**, 1845–1862 (2013).

19. C. E. Langlais, A. Lenton, R. Matear, D. Monselesan, B. Legresy, E. Cougnon, S. Rintoul, Stationary Rossby waves dominate subduction of anthropogenic carbon in the Southern Ocean. *Sci. Rep.* **7**, 17076 (2017).

20. K. Riahi, S. Rao, V. Krey, C. Cho, V. Chirkov, G. Fischer, G. Kindermann, N. Nakicenovic, P. Rafaj, RCP 8.5—A scenario of comparatively high greenhouse gas emissions. *Clim. Chang.* **109**, 33–57 (2011).

21. B. C. O'Neill, C. Tebaldi, D. P. van Vuuren, V. Eyring, P. Friedlingstein, G. Hurtt, R. Knutti, E. Kriegler, J.-F. Lamarque, J. Lowe, G. A. Meehl, R. Moss, K. Riahi, B. M. Sanderson, The scenario model intercomparison project (ScenarioMIP) for CMIP6. *Geosci. Model Dev.* **9**, 3461–3482 (2016).

22. R. Séférian, S. Berthet, A. Yool, J. Palmiéri, L. Bopp, A. Tagli-abue, L. Kwiatkowski, O. Aumont, J. Christian, J. Dunne, M. Gehlen, T. Ilyina, J. G. John, H. Li, M. Long, J. Y. Luo, H. Nakano, A. Romanou, J. Schwinger, C. Stock, Y. Santana-Falcón, Y. Takano, J. Tjiputra, H. Tsujino, M. Watanabe, T. Wu, F. Wu, A. Yamamoto, Tracking improvement in simulated marine biogeochemistry between CMIP5 and CMIP6. *Curr. Clim. Chang. Rep.* **6**, 95–119 (2020).

23. M. R. Allen, W. J. Ingram, Constraints on future changes in climate and the hydrologic cycle. *Nature* **419**, 228–232 (2002).

24. A. Hall, X. Qu, Using the current seasonal cycle to constrain snow albedo feedback in future climate change. *Geophys. Res. Lett.* **33**, GL025127 (2006).

25. A. Hall, P. Cox, C. Huntingford, S. Klein, Progressing emergent constraints on future climate change. *Nat. Clim. Change.* **9**, 269–278 (2019).

26. K. B. Tokarska, M. B. Stolpe, S. Sippel, E. M. Fischer, C. J. Smith, F. Lehner, R. Knutti, Past warming trend constrains future warming in CMIP6 models. *Sci. Adv.* **6**, eaaz9549 (2020).

27. F. J. M. M. Nijsse, P. M. Cox, M. S. Williamson, Emergent constraints on transient climate response (TCR) and equilibrium climate sensitivity (ECS) from historical warming in CMIP5 and CMIP6 models. *Earth Syst. Dynam.* **11**, 737–750 (2020).

28. P. M. Caldwell, M. D. Zelinka, S. A. Klein, Evaluating emergent constraints on equilibrium climate sensitivity. *J. Clim.* **31**, 3921–3942 (2018).

29. P. Cox, C. Huntingford, M. Williamson, Emergent constraint on equilibrium climate sensitivity from global temperature variability. *Nature* **553**, 319–322 (2018).

30. P. M. Cox, D. Pearson, B. B. Booth, P. Friedlingstein, C. Huntingford, C. D. Jones, C. M. Luke, Sensitivity of tropical carbon to climate change constrained by carbon dioxide variability. *Nature* **494**, 341–344 (2013).

31. S. Wenzel, P. M. Cox, V. Eyring, P. Friedlingstein, Emergent constraints on climate-carbon cycle feedbacks in the CMIP5 Earth system models. *J. Geophys. Res. Biogeosci.* **119**, 794–807 (2014).

32. L. Kwiatkowski, L. Bopp, O. Aumont, P. Ciais, P. M. Cox, C. Laufkötter, Y. Li, R. Séférian, Emergent constraints on projections of declining primary production in the tropical oceans. *Nat. Clim. Chang.* **7**, 355–358 (2017).

33. J. Terhaar, L. Kwiatkowski, L. Bopp, Emergent constraint on Arctic Ocean acidification in the twenty-first century. *Nature* **582**, 379–383 (2020).

34. F. Brient, Reducing uncertainties in climate projections with emergent constraints: Concepts, examples and prospects. *Adv. Atmos. Sci.* **37**, 1–15 (2020).

35. P. M. Caldwell, C. S. Bretherton, M. D. Zelinka, S. A. Klein, B. D. Santer, B. M. Sanderson, Statistical significance of climate sensitivity predictors obtained by data mining. *Geophys. Res. Lett.* **41**, 1803–1808 (2014).

36. V. Eyring, P. M. Cox, G. M. Flato, P. J. Gleckler, G. Abramowitz, P. Caldwell, W. D. Collins, B. K. Gier, A. D. Hall, F. M. Hoffman, G. C. Hurtt, A. Jahn, C. D. Jones, S. A. Klein, J. P. Krasting, L. Kwiatkowski, R. Lorenz, E. Maloney, G. A. Meehl, A. G. Pendergrass, R. Pincus, A. C. Ruane, J. L. Russell, B. M. Sanderson, B. D. Santer, S. C. Sherwood, I. R. Simpson, R. J. Stouffer, M. S. Williamson, Taking climate model evaluation to the next level. *Nat. Clim. Chang.* **9**, 102–110 (2019).

37. J. Marshall, K. Speer, Closure of the meridional overturning circulation through Southern Ocean upwelling. *Nat. Geosci.* **5**, 171–180 (2012).

38. L. D. Talley, Closure of the global overturning circulation through the Indian. Pacific and Southern Oceans: Schematics and transports. *Oceanography* **26**, 80–97 (2013).

39. T. DeVries, M. Holzer, F. Primeau, Recent increase in oceanic carbon uptake driven by weaker upper-ocean overturning. *Nature* **542**, 215–218 (2017).

40. T. Ito, M. Woloszyn, M. Mazloff, Anthropogenic carbon dioxide transport in the Southern Ocean driven by Ekman flow. *Nature* **463**, 80–83 (2010).

41. R. Séférian, D. Iudicone, L. Bopp, T. Roy, G. Madec, Water mass analysis of effect of climate change on air-sea CO_2 fluxes: The southern ocean. *J. Clim.* **25**, 3894–3908 (2012).

42. B. M. Sloyan, S. R. Rintoul, Circulation, renewal, and modification of Antarctic mode and intermediate water. *J. Phys. Oceanogr.* **31**, 1005–1030 (2001).

43. S. M. Downes, N. L. Bindoff, S. R. Rintoul, Impacts of climate change on the subduction of mode and intermediate water masses in the Southern Ocean. *J. Clim.* **22**, 3289–3302 (2009).

44. O. A. Saenko, A. Schmittner, A. J. Weaver, On the role of wind-driven sea ice motion on ocean ventilation. *J. Phys. Oceanogr.* **32**, 3376–3395 (2002).

45. V. Pellichero, J.-B. Sallée, C. C. Chapman, S. M. Downes, The southern ocean meridional overturning in the sea-ice sector is driven by freshwater fluxes. *Nat. Commun.* **9**, 1789 (2018).

46. J. Turner, T. J. Bracegirdle, T. Phillips, G. J. Marshall, J. S. Hosking, An initial assessment of Antarctic sea ice extent in the CMIP5 models. *J. Clim.* **26**, 1473–1484 (2013).

47. A. Purich, M. H. England, W. Cai, A. Sullivan, P. J. Durack, Impacts of broad-scale surface freshening of the Southern Ocean in a coupled climate model. *J. Clim.* **31**, 2613–2632 (2018).

48. T. J. Bracegirdle, E. Shuckburgh, J.-B. Sallee, Z. Wang, A. J. S. Meijers, N. Bruneau, T. Phillips, L. J. Wilcox, Assessment of surface winds over the Atlantic, Indian, and Pacific Ocean sectors of the Southern Ocean in CMIP5 models: Historical bias, forcing response, and state dependence. *J. Geophys. Res.* **118**, 547–562 (2013).

49. J. K. Moore, M. R. Abbott, J. G. Richman, Location and dynamics of the Antarctic polar front from satellite sea surface temperature data. *J. Geophys. Res.* **104**, 3059–3073 (1999).

50. S. R. Rintoul, J. R. Donguy, D. H. Roemmich, Seasonal evolution of upper ocean thermal structure between Tasmania and Antarctica. *Deep-Sea Res. I* **44**, 1185–1202 (1997).

51. A. H. Orsi, T. I. I. I. Whitworth, W. D. J. Nowlin Jr., On the meridional extent and fronts of the Antarctic Circumpolar Current. *Deep-Sea Res. I* **42**, 641–673 (1995).

52. M. Meinshausen, S. J. Smith, K. Calvin, J. S. Daniel, M. Kainuma, J.-F. Lamarque, K. Matsumoto, S. Montzka, S. Raper, K. Riahi, A. Thomson, G. J. M. Velders, D. P. P. van Vuuren, The RCP greenhouse gas concentrations and their extensions from 1765 to 2300. *Clim. Chang.* **109**, 213–241 (2011).

53. M. Meinshausen, Z. Nicholls, J. Lewis, M. J. Gidden, E. Vogel, M. Freund, U. Beyerle, C. Gessner, A. Nauels, N. Bauer, J. G. Canadell, J. S. Daniel, A. John, P. Krummel, G. Luderer, N. Meinshausen, S. A. Montzka, S. J. Smith, M. van den Berg, G. J. M. Velders, M. Vollmer, H. J. Wang, The SSP greenhouse gas concentrations and their extensions to 2500. *Geosci. Model Dev. Discuss.* **2019**, 1–77 (2019).

54. J. C. Orr, V. J. Fabry, O. Aumont, L. Bopp, S. C. Doney, R. A. Feely, A. Gnanadesikan, N. Gruber, A. Ishida, F. Joos, R. M. Key, K. Lindsay, E. Maier-Reimer, R. Matear, P. Monfray, A. Mouchet, R. G. Najjar, G.-K. Plattner, K. B. Rodgers, C. L. Sabine, J. L. Sarmiento, R. Schlitzer, R. D. Slater, I. J. Totterdell, M.-F. Weirig, Y. Yamanaka, A. Yool, Anthropogenic ocean acidification over the twenty-first century and its impact on calcifying organisms. *Nature* **437**, 681–686 (2005).

55. V. J. Fabry, J. B. McClintock, J. T. Mathis, J. M. Grebmeier, Ocean acidification at high latitudes: The Bellwether. *Oceanography* **22**, 160–171 (2009).

56. J.-P. Gattuso, L. Hansson, *Ocean Acidification* (Oxford Univ. Press, 2011).

57. K. J. Kroeker, R. L. Kordas, R. Crim, I. E. Hendriks, L. Ramajo, G. S. Singh, C. M. Duarte, J. P. Gattuso, Impacts of ocean acidification on marine organisms: Quantifying sensitivities and interaction with warming. *Glob. Chang. Biol.* **9**, 1884–1896 (2013).

58. Z. Lachkar, J. C. Orr, J.-C. Dutay, P. Delecluse, Effects of mesoscale eddies on global ocean distributions of CFC-11, CO_2, and $\Delta^{14}C$. *Ocean Sci.* **3**, 461–482 (2007).

59. Z. Lachkar, J. C. Orr, J.-C. Dutay, Seasonal and mesoscale variability of oceanic transport of anthropogenic CO_2. *Biogeosciences* **6**, 2509–2523 (2009).

60. C. O. Dufour, S. M. Griffies, G. F. de Souza, I. Frenger, A. K. Morrison, J. B. Palter, J. L. Sarmiento, E. D. Galbraith, J. P. Dunne, W. G. Anderson, R. D. Slater, Role of mesoscale eddies in cross-frontal transport of heat and biogeochemical tracers in the Southern Ocean. *J. Phys. Oceanogr.* **45**, 3057–3081 (2015).

61. S. M. Griffies, M. Winton, W. G. Anderson, R. Benson, T. L. Delworth, C. O. Dufour, J. P. Dunne, P. Goddard, A. K. Morrison, A. Rosati, A. T. Wittenberg, J. Yin, R. Zhang, Impacts on ocean heat from transient mesoscale eddies in a hierarchy of climate models. *J. Clim.* **28**, 952–977 (2015).

62. R. Hallberg, Using a resolution function to regulate parameterizations of oceanic mesoscale eddy effects. *Ocean Model* **72**, 92–103 (2013).

63. H. T. Hewitt, M. Roberts, P. Mathiot, A. Biastoch, E. Blockley, E. P. Chassignet, B. Fox-Kemper, P. Hyder, D. P. Marshall, E. Popova, A.-M. Treguier, L. Zanna, A. Yool, Y. Yu, R. Beadling, M. Bell, T. Kuhlbrodt, A. Arsouze, A. Bellucci, F. Castruccio, B. Gan, D. Putrasahan, C. D. Roberts, L. Van Roekel, Q. Zhang, Resolving and parameterising the ocean mesoscale in Earth system models. *Curr. Clim. Chang. Rep.* **6**, 137–152 (2020).

64. A. S. Gupta, N. C. Jourdain, J. N. Brown, D. Monselesan, Climate drift in the CMIP5 models. *J. Clim.* **26**, 8597–8615 (2013).

65. R. Séférian, M. Gehlen, L. Bopp, L. Resplandy, J. C. Orr, O. Marti, J. P. Dunne, J. R. Christian, S. C. Doney, T. Ilyina, K. Lindsay, P. R. Halloran, C. Heinze, J. Segschneider, J. Tjiputra, O. Aumont, A. Romanou, Inconsistent strategies to spin up models in CMIP5: Implications for ocean biogeochemical model performance assessment. *Geosci. Model Dev.* **9**, 1827–1851 (2016).

66. B. Bronselaer, J. L. Russell, M. Winton, N. L. Williams, R. M. Key, J. P. Dunne, R. A. Feely, K. S. Johnson, J. L. Sarmiento, Importance of wind and meltwater for observed chemical and physical changes in the Southern Ocean. *Nat. Geosci.* **13**, 35–42 (2020).

67. N. S. Lovenduski, N. Gruber, S. C. Doney, Toward a mechanistic understanding of the decadal trends in the Southern Ocean carbon sink. *Glob. Biogeochem. Cycles* **22**, GB3016 (2008).

68. L. Bopp, L. Resplandy, J. C. Orr, S. C. Doney, J. P. Dunne, M. Gehlen, P. Halloran, C. Heinze, T. Ilyina, R. Séférian, J. Tjiputra, M. Vichi, Multiple stressors of ocean ecosystems in the 21st century: Projections with CMIP5 models. *Biogeosciences* **10**, 6225–6245 (2013).

69. L. Kwiatkowski, O. Torres, L. Bopp, O. Aumont, M. Chamberlain, J. R. Christian, J. P. Dunne, M. Gehlen, T. Ilyina, J. G. John, A. Lenton, H. Li, N. S. Lovenduski, J. C. Orr, J. Palmieri, Y. Santana-Falcón, J. Schwinger, R. Séférian, C. A. Stock, A. Tagliabue, Y. Takano, J. Tjiputra, K. Toyama, H. Tsujino, M. Watanabe, A. Yamamoto, A. Yool, T. Ziehn, Twenty-first century ocean warming, acidification, deoxygenation, and upper-ocean nutrient and primary production decline from CMIP6 model projections. *Biogeosciences* **17**, 3439–3470 (2020).

70. P. Landschützer, N. Gruber, F. Alexander Haumann, C. Rödenbeck, D. C. E. Bakker, S. van Heuven, M. Hoppema, N. Metzl, C. Sweeney, T. Takahashi, B. Tilbrook, R. Wanninkhof, The reinvigoration of the Southern Ocean carbon sink. *Science* **349**, 1221–1224 (2015).

71. J. Terhaar, J. C. Orr, M. Gehlen, C. Ethé, L. Bopp, Model constraints on the anthropogenic carbon budget of the Arctic Ocean. *Biogeosciences* **16**, 2343–2367 (2019).

72. J. Hauck, C. Völker, D. A. Wolf-Gladrow, C. Laufkötter, M. Vogt, O. Aumont, L. Bopp, E. T. Buitenhuis, S. C. Doney, J. Dunne, N. Gruber, T. Hashioka, J. John, C. L. Quéré, I. D. Lima, H. Nakano, R. Séférian, I. Totterdell, On the Southern Ocean CO_2 uptake and the role of the biological carbon pump in the 21st century. *Glob. Biogeochem. Cycles* **29**, 1451–1470 (2015).

73. R. Beadling, J. Russell, R. Stouffer, M. Mazloff, L. Talley, P. Goodman, J. Sallée, H. Hewitt, P. Hyder, A. Pandde, Representation of southern ocean properties across coupled model intercomparison project generations: CMIP3 to CMIP6. *J. Clim.* **33**, 6555–6581 (2020).

74. D. Swingedouw, J. Mignot, P. Braconnot, E. Mosquet, M. Kageyama, R. Alkama, Impact of freshwater release in the north atlantic under different climate conditions in an OAGCM. *J. Clim.* **22**, 6377–6403 (2009).

75. R. Abernathey, I. Cerovecki, P. Holland, E. Newsom, M. Mazloff, L. D. Talley, Water-mass transformation by sea ice in the upper branch of the Southern Ocean overturning. *Nat. Geosci.* **9**, 596–601 (2016).

76. F. Haumann, N. Gruber, M. Münnich, I. Frenger, S. Kern, Sea-ice transport driving Southern Ocean salinity and its recent trends. *Nature* **537**, 89–92 (2016).

77. J. C. Orr, J.-M. Epitalon, Improved routines to model the ocean carbonate system: mocsy 2.0. *Geosci. Model Dev.* **8**, 485–499 (2015).

78. A. G. Dickson, C. L. Sabine, J. R. Christian, *Guide to Best Practices For Ocean CO2 Measurements191* (PICES Special Publication 3, 2007).

79. S. K. Lauvset, R. M. Key, A. Olsen, S. van Heuven, A. Velo, X. Lin, C. Schirnick, A. Kozyr, T. Tanhua, M. Hoppema, S. Jutterström, R. Steinfeldt, E. Jeansson, M. Ishii, F. F. Perez, T. Suzuki, S. Watelet, A new global interior ocean mapped climatology: The 1°×1° GLODAP version 2. *Earth Syst. Sci. Data* **8**, 325–340 (2016).

80. T. P. Boyer, H. E. Garcia, R. A. Locarnini, M. M. Zweng, A. V. Mishonov, J. R. Reagan, K. A. Weathers, O. K. Baranova, D. Seidov, I. V. Smolyar, (World Ocean Atlas 2018). [Temperature, Salinity]. NOAA National Centers for Environmental Information. Dataset. Accessed March 2019; https://accession.nodc.noaa.gov/NCEI-WOA18.

81. M. Gloor, N. Gruber, J. Sarmiento, C. L. Sabine, R. A. Feely, C. Rodenbeck, A first estimate of present and preindustrial air-sea CO2 flux patterns based on ocean interior carbon measurements and models. *Geophys. Res. Lett.* **30**, 10-1–10-4 (2003).

82. B. Bronselaer, M. Winton, J. Russell, C. L. Sabine, S. Khatiwala, Agreement of CMIP5 simulated and observed ocean anthropogenic CO_2 uptake. *Geophys. Res. Lett.* **44**, 12298–12305 (2017).

83. J.-L. Dufresne, M.-A. Foujols, S. Denvil, A. Caubel, O. Marti, O. Aumont, Y. Balkanski, S. Bekki, H. Bellenger, R. Benshila, S. Bony, L. Bopp, P. Braconnot, P. Brockmann, P. Cadule, F. Cheruy, F. Codron, A. Cozic, D. Cugnet, N. de Noblet, J.-P. Duvel, C. Ethé, L. Fairhead, T. Fichefet, S. Flavoni, P. Friedlingstein, J.-Y. Grandpeix, E. Guez, E. Guilyardi, D. Hauglustaine, F. Hourdin, A. Idelkadi, J. Ghattas, S. Joussaume, M. Kageyama, G. Krinner, S. Labetoulle, A. Lahellec, M.-P. Lefebvre, F. Lefevre, C. Levy, Z. X. Li, J. Lloyd, F. Lott, G. Madec, M. Mancip, M. Marchand, S. Masson, Y. Meurdesoif, J. Mignot, I. Musat, S. Parouty, J. Polcher, C. Rio, M. Schulz, D. Swingedouw, S. Szopa, C. Talandier, P. Terray, N. Viovy, N. Vuichard, Climate change projections using the IPSL-CM5 Earth system model: From CMIP3 to CMIP5. *Clim. Dyn.* **40**, 2123–2165 (2013).

84. F. Hourdin, A. Jam, C. Rio, F. Couvreux, I. Sandu, M.-P. Lefebvre, F. Brient, A. Idelkadi, Unified parameterization of convective boundary layer transport and clouds with the thermal plume model. *J. Adv. Model. Earth Syst.* **11**, 2910–2933 (2019).

85. J. P. Dunne, J. G. John, A. J. Adcroft, S. M. Griffies, R. W. Hallberg, E. Shevliakova, R. J. Stouffer, W. Cooke, K. A. Dunne, M. J. Harrison, J. P. Krasting, S. L. Malyshev, P. C. D. Milly, P. J. Phillipps, L. T. Sentman, B. L. Samuels, M. J. Spelman, M. Winton, A. T. Wittenberg, N. Zadeh, GFDL's ESM2 global coupled climate–carbon Earth system models. Part I: Physical formulation and baseline simulation characteristics. *J. Clim.* **25**, 6646–6665 (2012).

86. I. M. Held, H. Guo, A. Adcroft, J. P. Dunne, L. W. Horowitz, J. Krasting, E. Shevliakova, M. Winton, M. Zhao, M. Bushuk, A. T. Wittenberg, B. Wyman, B. Xiang, R. Zhang, W. Anderson, V. Balaji, L. Donner, K. Dunne, J. Durachta, P. P. G. Gauthier, P. Ginoux, J.-C. Golaz, S. M. Griffies, R. Hallberg, L. Harris, M. Harrison, W. Hurlin, J. John, P. Lin, S.-J. Lin, S. Malyshev, R. Menzel, P. C. D. Milly, Y. Ming, V. Naik, D. Paynter, F. Paulot, V. Rammaswamy, B. Reichl, T. Robinson, A. Rosati, C. Seman, L. G. Silvers, S. Underwood, N. Zadeh, Structure and performance of GFDL's CM4.0 climate model. *J. Adv. Model. Earth Syst.* **11**, 3691–3727 (2019).

87. M. A. Giorgetta, J. Jungclaus, C. H. Reick, S. Legutke, J. Bader, M. Böttinger, V. Brovkin, T. Crueger, M. Esch, K. Fieg, K. Glushak, V. Gayler, H. Haak, H.-D. Hollweg, T. Ilyina, S. Kinne, L. Kornblueh, D. Matei, T. Mauritsen, U. Mikolajewicz, W. Mueller, D. Notz, F. Pithan, T. Raddatz, S. Rast, R. Redler, E. Roeckner, H. Schmidt, R. Schnur, J. Segschneider, K. D. Six, M. Stockhause, C. Timmreck, J. Wegner, H. Widmann, K.-H. Wieners, M. Claussen, J. Marotzke, B. Stevens, Climate and carbon cycle changes from 1850 to 2100 in MPI-ESM simulations for the Coupled Model Intercomparison Project phase 5. *J. Adv. Model. Earth Syst.* **5**, 572–597 (2013).

88. O. Gutjahr, D. Putrasahan, K. Lohmann, J. H. Jungclaus, J. S. von Storch, N. Brüggemann, H. Haak, A. Stössel, Max Planck Institute Earth System Model (MPI-ESM1.2) for the High-Resolution Model Intercomparison Project (HighResMIP). *Geosci. Model Dev.* **12**, 3241–3281 (2019).

89. W. J. Collins, N. Bellouin, M. Doutriaux-Boucher, N. Gedney, P. Halloran, T. Hinton, J. Hughes, C. D. Jones, M. Joshi, S. Liddicoat, G. Martin, F. O'Connor, J. Rae, C. Senior, S. Sitch, I. Totterdell, A. Wiltshire, S. Woodward, Development and evaluation of an Earth-System model—HadGEM2. *Geosci. Model Dev.* **4**, 1051–1075 (2011).

90. A. A. Sellar, J. Walton, C. G. Jones, R. Wood, N. L. Abraham, M. Andrejczuk, M. B. Andrews, T. Andrews, A. T. Archibald, L. de Mora, H. Dyson, M. Elkington, R. Ellis, P. Florek, P. Good, L. Gohar, S. Haddad, S. C. Hardiman, E. Hogan, A. Iwi, C. D. Jones, B. Johnson, D. I. Kelley, J. Kettleborough, J. R. Knight, M. O. Köhler, T. Kuhlbrodt, S. Liddicoat, I. Linova-Pavlova, M. S. Mizielinski, O. Morgenstern, J. Mulcahy, E. Neininger, F. M. O'Connor, R. Petrie, J. Ridley, J.-C. Rioual, M. Roberts, E. Robertson, S. Rumbold, J. Seddon, H. Shepherd, S. Shim, A. Stephens, J. C. Teixiera, Y. Tang, J. Williams, A. Wiltshire, P. T. Griffiths, Implementation of U.K. Earth system models for CMIP6. *J. Adv. Model. Earth Syst.* **12**, 1–27 (2020).

91. S. Watanabe, T. Hajima, K. Sudo, T. Nagashima, T. Takemura, H. Okajima, T. Nozawa, H. Kawase, M. Abe, T. Yokohata, H. Ise, H. Sato, E. Kato, K. Takata, S. Emori, M. Kawamiya, MIROC-ESM 2010: Model description and basic results of CMIP5-20c3m experiments. *Geosci. Model Dev.* **4**, 845–872 (2011).

92. T. Hajima, M. Watanabe, A. Yamamoto, H. Tatebe, M. A. Noguchi, M. Abe, R. Ohgaito, A. Ito, D. Yamazaki, H. Okajima, A. Ito, K. Takata, K. Ogochi, S. Watanabe, M. Kawamiya, Description of the MIROC-ES2L Earth system model and evaluation of its climate–biogeochemical processes and feedbacks. *Geosci. Model Dev. Discuss.*, (2019).

93. M. Bentsen, I. Bethke, J. B. Debernard, T. Iversen, A. Kirkevåg, Ø. Seland, H. Drange, C. Roelandt, I. A. Seierstad, C. Hoose, J. E. Kristjansson, The Norwegian Earth System Model, NorESM1-M – Part 1: Description and basic evaluation of the physical climate. *Geosci. Model Dev.* **6**, 687–720 (2013).

94. J. F. Tjiputra, J. Schwinger, M. Bentsen, A. L. Morée, S. Gao, I. Bethke, C. Heinze, N. Goris, A. Gupta, Y.-C. He, D. Olivié, Ø. Seland, M. Schulz, Ocean biogeochemistry in the Norwegian Earth System Model version 2 (NorESM2). *Geosci. Model Dev.* **13**, 2393–2431 (2020).

95. P. G. Fogli, D. Iovino, "CMCC–CESM–NEMO: Toward the new CMCC Earth system model," *CMCC Research Paper* (no. 248) (2014).

96. P. R. Gent, G. Danabasoglu, L. J. Donner, M. M. Holland, E. C. Hunke, S. R. Jayne, D. M. Lawrence, R. B. Neale, P. J. Rasch, M. Vertenstein, P. H. Worley, Z.-L. Yang, M. Zhang, The community climate system model version 4. *J. Clim.* **24**, 4973–4991 (2011).

97. K. Lindsay, G. B. Bonan, S. C. Doney, F. M. Hoffman, D. M. Lawrence, M. C. Long, N. M. Mahowald, J. Keith Moore, J. T. Randerson, P. E. Thornton, Preindustrial-control and twentieth-century carbon cycle experiments with the Earth system model CESM1(BGC). *J. Clim.* **27**, 8981–9005 (2014).

98. G. Danabasoglu, J.-F. Lamarque, J. Bacmeister, D. A. Bailey, A. K. DuVivier, J. Edwards, L. K. Emmons, J. Fasullo, R. G. A. Gettelman, C. Hannay, M. M. Holland, W. G. Large, P. H. Lauritzen, D. M. Lawrence, J. T. M. Lenaerts, K. Lindsay, W. H. Lipscomb, M. J. Mills, R. Neale, K. W. Oleson, B. Otto-Bliesner, A. S. Phillips, W. Sacks, S. Tilmes, L. van Kampenhout, M. Vertenstein, A. Bertini, J. Dennis, C. Deser, C. Fischer, B. Fox-Kemper, J. E. Kay, D. Kinnison, P. J. Kushner, V. E. Larson, M. C. Long, S. Mickelson, J. K. Moore, E. Nienhouse, L. Polvani, P. J. Rasch, W. G. Strand, The Community Earth System Model version 2 (CESM2). *J. Adv. Model. Earth Syst.* **12**, 1–35 (2020).

99. N. C. Swart, J. N. S. Cole, V. V. Kharin, M. Lazare, J. F. Scinocca, N. P. Gillett, J. Anstey, V. Arora, J. R. Christian, S. Hanna, Y. Jiao, W. G. Lee, F. Majaess, O. A. Saenko, C. Seiler, C. Seinen, A. Shao, M. Sigmond, L. Solheim, K. von Salzen, D. Yang, B. Winter, The Canadian Earth system model version 5 (CanESM5.0.3). *Geosci. Model Dev.* **12**, 4823–4873 (2019).

100. R. Séférian, P. Nabat, M. Michou, D. Saint-Martin, A. Voldoire, J. Colin, B. Decharme, C. Delire, S. Berthet, M. Chevallier, S. Sénési, L. Franchisteguy, J. Vial, M. Mallet, E. Joetzjer, O. Geoffroy, J.-F. Guérémy, M.-P. Moine, R. Msadek, A. Ribes, M. Rocher, R. Roehrig, D. Salas-y-Mélia, E. Sanchez, L. Terray, S. Valcke, R. Waldman, O. Aumont, L. Bopp, J. Deshayes, G. Éthé, G. Madec, Evaluation of CNRM Earth system model, CNRM-ESM2-1: Role of Earth system processes in present-day and future climate. *J. Adv. Model. Earth Syst.* **11**, 4182–4227 (2019).

Citation: J. Terhaar, T. L. Frölicher, F. Joos, Southern Ocean anthropogenic carbon sink constrained by sea surface salinity. *Sci. Adv.* **7**, eabd5964 (2021).

Science Advances

Southern Ocean anthropogenic carbon sink constrained by sea surface salinity

Jens Terhaar, Thomas L. Frölicher and Fortunat Joos

ARTICLE TOOLS	http://advances.sciencemag.org/content/7/18/eabd5964
SUPPLEMENTARY MATERIALS	http://advances.sciencemag.org/content/suppl/2021/04/26/7.18.eabd5964.DC1
REFERENCES	This article cites 95 articles, 5 of which you can access for free http://advances.sciencemag.org/content/7/18/eabd5964#BIBL
PERMISSIONS	http://www.sciencemag.org/help/reprints-and-permissions

Use of this article is subject to the Terms of Service